



Cobalt-intercalated one-dimensional nanocrystals of urea perylene imide polymer for enhanced visible-light photocatalytic water oxidation

Aihui Cao ^{a,b,c}, Renfu Li ^a, Xiao Xu ^{a,b}, Weifeng Huang ^{a,b}, Ying He ^{a,b,c}, Junqiang Li ^{a,b}, Miao Sun ^{a,b}, Xueyuan Chen ^a, Longtian Kang ^{a,b,*}

^a Key Laboratory of Design and Assembly of Functional Nanostructures, and Fujian Provincial Key Laboratory of Nanomaterials, Fujian Institute of Research on the Structure of Matter, Chinese Academy of Sciences, Fuzhou, Fujian 350002, PR China

^b Fujian Science & Technology Innovation Laboratory for Optoelectronic Information of China, Fuzhou, Fujian 350108, PR China

^c University of Chinese Academy of Sciences, Chinese Academy of Sciences, Beijing 100049, PR China



ARTICLE INFO

Keywords:

Photocatalysis

Urea perylene imide

Cobaltous nitrate

One-dimensional nanocrystal

Water oxidation

ABSTRACT

Urea perylene imide polymer (UPDI) is successfully recombined with $\text{Co}(\text{NO}_3)_2$ molecules into one-dimensional nanocrystals (Co-UPDI) for enhanced photocatalytic oxygen evolution (POE) under visible light. Co-UPDI as photocatalyst exhibits more an order of magnitude of POE rate than UPDI at $\text{pH} = 4.8$ (8.00 vs. 0.58 $\text{mmol h}^{-1}\text{g}^{-1}$), which is the highest among reported POE tests in aqueous colloid system with AgNO_3 as sacrificial agent. The apparent quantum yield (AQY) reaches 4.39 % at 450 nm. The systematical experiments reveals that the heterojunction formation between UPDI line and $\text{Co}(\text{NO}_3)_2$ molecules is crucial through the coordination of Co with N atoms. Consequently, the rigidity of UPDI line enhances, H-type stacking of PDI moiety becomes closer, and CoOOH as cocatalyst in-situ forms during POE. Meanwhile, more excitons with longer lifetime generate and more quickly transfer in Co-UPDI than UPDI nanocrystals. This work provides an efficient strategy for photocatalytic water oxidation.

1. Introduction

The artificial photosynthesis, e.g. through the photocatalysis of overall water or CO_2 splitting, has been considered as a promising strategy to achieve carbon neutrality [1–7]. During the photocatalytic process, both reduction and oxidation reactions can be designed to directly transform the solar energy into the useful chemicals. In two half reactions, the POE is usually sluggish and the rate-controlling step due to the 4e-process of water oxidation [8]. At present, an efficient way is to use semiconductor materials with suitable energy level. The influence of conventional semiconductors, such as TiO_2 , BiVO_4 , Fe_2O_3 , $\text{g-C}_3\text{N}_4$ etc., in POE process has been widely investigated because of their non-toxicity, cheap and high stability [5]. However, most of these typical materials with short exciton lifetime and low charge carrier mobility only absorb the limited solar visible light, leading to their intrinsic poor photocatalytic activity. A variety of complicated methods, e.g. designing defects, doping or building heterojunction [9–12] etc., have to be used to enhance their activity. Recently, the molecule-based semiconductors, e.g. p-type phthalocyanine and porphyrin [13,14],

n-type condensed aromatics [15] and donor-acceptor complexes [16], attract the increasing attentions for efficient photocatalytic water splitting owing to intrinsic wide visible light absorption, easily modified structure and adjustable property. Among them, the perylene-based materials with low HOMO energy level (vs. Vac.) and quick electron-dominated carriers exhibit a huge advantage on POE process.

Perylene diimide (PDI) and its derivative, as typical n-type π -conjugate organic semiconductors, have a potential photocatalytic activity due to high photochemical stability under visible light [17–20]. However, the weak ability of photoelectric conversion usually restricts its activity because of short lifetime and transportation distance of Frenkel exciton [21]. Up to now, four ways have been proved efficient to promote the generation, transportation and separation of photoinduced carriers. 1) To improve the intramolecular built-in electric field via the linkage of different functional groups, such as $-\text{COOH}$, $-\text{NH}_2$, and $-\text{H}_2\text{POO}_3$ etc. [18,22], may achieve the spatial symmetry-breaking charge separation and promote charge transfer [23]. Zhu's group reported that the introduction of $-\text{COOH}$ or urea group into PDI was helpful for the charge separation and water oxidation [23,24]. 2) To

* Correspondence to: Fujian Institute of Research on the Structure of Matter, Chinese Academy of Sciences, Fuzhou, Fujian 350002, PR China.
E-mail address: longtiank@fjirsm.ac.cn (L. Kang).

form aggregate or supramolecule structure, especially H-type aggregate, may significantly extent the light absorption and prolong exciton lifetime due to the electron-coupling [25]. 3) To link PDI group with metal atoms, e.g. Zn, Fe, Co, and Ni etc., can change the transportation path of photoinduced carriers, prolong the triplet-state exciton lifetime and even enhance the interfacial reaction. Duan et al. proved that one-dimensional (1D) nanostructure of Zn-PDI had the high activity of photocatalytic oxidation owing to the rapid electron transfer [26]. Our group also achieved the highest POE rate in aqueous colloid system basing on 1D Co-PDI nanocrystals [27]. 4) To construct heterostructure, such as Z-scheme structure [7,11], is a common strategy for improving the catalytic performance. By this way, not only the photoelectric conversion can be increased, but also the interfacial reaction and stability can be enhanced. The precious metals iridium or ruthenium oxide as cocatalyst is usually applied in the catalysis of water oxidation [28]. However, more economical way is to in-situ generate non-precious compounds with high catalytic activity for OER, e.g. CoOOH and FeOOH etc. [27,29].

Even so, the photocatalytic process is a systematic and complicated engineering. It is not enough for us to improve the catalytic performance through only one or two ways. For example, UPDI with a strong built-in electric field exhibits outstanding POE activity owing to high thermodynamic potential energy, which benefits to the intramolecular charge transfer [23]. However, the flexible C–N bond and inefficient local tunneling effect seriously limit the exciton transportation in its crystal [30]. Can we achieve more highly efficient photocatalysis for PDI-based POE, simultaneously using the above strategies through a simple synthetic method? As a result, it can enhance the solar visible-light absorption, generate and efficiently transport more photoinduced carrier with long lifetime, and in-situ form the non-precious cocatalyst with high reaction activity. Up to date, this is still a huge challenge. In this work, the synthesis of Co-doped UPDI was explored through the intercalation of $\text{Co}(\text{NO}_3)_2$ molecules into 1D UPDI crystal by a mild hydrothermal reaction. A large amount of 1D Co–UPDI nanocrystals with good water dispersibility can be obtained. The systematical experiments were carried out to investigate the morphology, structure, components and formation mechanism of Co–UPDI nanocrystals. The photoelectric conversion, electrocatalytic property and POE activity of 1D UPDI and Co–UPDI nanocrystals were comprehensively compared and analyzed. As compare with UPDI nanorods (NRs), Co–UPDI NRs exhibit better POE activity (0.58 vs. 8.0 $\text{mmol h}^{-1} \text{g}^{-1}$) with AgNO_3 as electron acceptor. The effect of Co doping in UPDI on the photoelectric conversion and interfacial reaction was evaluated. Furthermore, the difference between UPDI and Co-UDPI in the photoelectric conversion was revealed through the femtosecond transient absorption (fsTA) spectra.

2. Experimental section

2.1. Chemicals

3,4,9,10–Perylenetetracarboxylic dianhydride (PDA) and imidazole were obtained from J&K Chemicals Co. Urea ($\text{CH}_4\text{N}_2\text{O}$), anhydrous zinc acetate $\text{C}_4\text{H}_6\text{O}_4\text{Zn}$, cobaltous nitrate hexahydrate ($\text{Co}(\text{NO}_3)_2 \cdot 6 \text{H}_2\text{O}$), hydrochloric acid (HCl), silver nitrate (AgNO_3) and triethylamine (TEA, $\text{C}_6\text{H}_{15}\text{N}$) etc. were purchased from Sinopharm Chemical Reagent Co., Ltd. (shanghai, China). The ultrapure water was produced with a Water Purifier apparatus (WP-UP-IV-20).

2.2. Synthesis of 1D UPDI nanocrystals

The UPDI was synthesized according to the reported literature [31]. In a typical process, imidazole (5 g), perylene 3,4,9,10-tetracarboxylic dianhydride (2.0 mmol), urea (2.0 mmol) and anhydrous zinc acetate were added into 100 mL three necked flask, and then were heated at 140 °C for 5 h under argon atmosphere. After reaction, the product was dissolved in 250 mL HCl (1.0 M). Crude solid sample was collected by

the centrifugation at 10,000 rpm for 10 min. The solid was washed by boil NaHCO_3 solution for several times, and then was dried at 70 °C. Finally, the product was thoroughly washed using DMSO aqueous solution. The as-obtained sample was kept for further using and named as urea PDI (UPDI).

2.3. Synthesis of 1D Co–UPDI nanocrystals

The Co–UPDI was synthesized under a hydrothermal condition. In a typical experiment, 16 mg UPDI was firstly dispersed into 14.0 mL of $\text{H}_2\text{O}/\text{DMF}$ solution ($V_{\text{H}_2\text{O}}: V_{\text{DMF}} = 5:2$) containing 6 μL of TEA as dispersing agent. Then, 0.064 mmol $\text{Co}(\text{NO}_3)_2 \cdot 6\text{H}_2\text{O}$ aqueous solution was dropped into the above UPDI dispersed system with stirring to form a uniform mixed system. Finally, the mixture was transferred to 20 mL glass bottle, and heated at 120 °C for 3 days. After that temperature was slowly cooled to room temperature, the precipitate was collected and washed with ethanol/water solution for several times. The dark red sample was named as cobalt urea PDI (Co–UPDI) after drying for further analysis.

2.4. Synthesis of CoOOH and CoOOH/UPDI

According to the previous report [32], cobalt hydroxide oxide (CoOOH) was synthesized by hydrothermal and in situ oxidation methods. Firstly, 2.1 mmol $\text{Co}(\text{NO}_3)_2 \cdot 6\text{H}_2\text{O}$ was dissolved in 200 mL mix solution of water and glycol solution with the volume ratio of 1:1. Then, 5.0 M ammonia water solution was dropped to adjust the pH value to 10. Subsequently, the above solution was transferred to a reaction kettle, and then heated at 130 °C for 10 h. After cooling to room temperature, the above system was separated and washed. The brown precipitate can be obtained. After the precipitate was dispersed in 100 mL water again, 0.5 M NaClO solution was dropped until the precipitate completely formed at 50 °C. After one hour, the precipitate was separated and repeatedly washed with a large amount of UW. The CoOOH powder can be obtained after vacuum drying for further use. Through the above same method, the CoOOH/UPDI composite was also synthesized with the existence of UPDI. In order to compare with the synthesis of Co-UPDI, the amount of UPDI and $\text{Co}(\text{NO}_3)_2 \cdot 6\text{H}_2\text{O}$ was still 16 mg and 0.064 mmol, respectively.

2.5. Measurement of the photocatalytic activity

Typically, 10 mg catalyst was dispersed in 100 mL water, including 5.0 mM AgNO_3 as sacrificial reagents, to form a colloid system through stirring. In the cycling test, the Co-UPDI NRs as photocatalyst was firstly separated by the centrifugation at 10,000 rpm for 10 min, and then was washed with dilute nitric acid (pH= 4.8) to remove the generated Ag and CoOOH. A new photocatalytic system was built with these Co-UPDI NRs and 5.0 mM AgNO_3 . Subsequently, the mixture was transferred into the photocatalytic reaction vessel. The glass reactor was connected with the photocatalytic system (Perfect Light, Labsolar-6A) and degassed under vacuum condition for 20 min. The POE test was carried under the irradiation of a 300 W Xe lamp (Perfect Light, PLS-SXE300BF) with 420-nm cut-off filter. The amount of generated oxygen gas in the reactor was automatically collected and on-line detected with an on-line gas chromatograph (Techcomp, GC7900) every 20 min during 120-min test.

The photocatalytic activity was measured at the wavelength of 420, 450, 500, 550, 600, 650 and 700 nm. Then the AQY was calculated according to the following formula, respectively.

$$\begin{aligned} \text{AQY}(\%) &= \frac{4 \times \text{number of evolved } \text{O}_2 \text{ molecules}}{\text{number of incident photons}} \\ &= \frac{4 \times n \times NA}{S \times P \times t \times \frac{\lambda}{h \times c}} \\ &= \frac{4 \times n \times NA \times hc}{S \times P \times t \times \lambda} \end{aligned}$$

Where n stands for the O_2 molar amount (μmol), N_A represents Avogadro constant ($6.02 \times 10^{23} / \text{mol}$), S is the irradiation area (26.4 cm^2), P is the light intensity (mW cm^{-2}) detected with optical power meter, t is the light irradiation time (s), λ is the light wavelength (nm), h is $6.626 \times 10^{-34} \text{ Js}$, c is the light speed of $3 \times 10^8 \text{ m/s}$.

2.6. Photoelectrochemical measurement

Conventional standard three-electrode system was used for the electrochemical test in $0.5 \text{ M Na}_2\text{SO}_4$ solution, including counter electrode (Carbon rod), reference electrode (Ag/AgCl electrode) and working electrode. The working electrode was prepared by the following steps. 5.0 mg sample was ultrasonically dispersed into 1.0 mL of Nafion/ H_2O solution ($V_N: V_H = 1:9$) for 30 min to form a uniform suspension, then was coated on ITO conductive glass ($1.5 \text{ cm}^2 \times 1.5 \text{ cm}$). The ITO glass was dried under vacuum condition at 50°C for 24 h . Last, the three electrodes were assembled and tested on a CHI760E electrochemical workstation (Chenhua Instruments, Shanghai, China). During photocurrent test, the light source was 300 W Xe lamp ($\lambda > 420 \text{ nm}$). In our electrochemical impedance test, $80 \mu\text{L}$ of sample, e.g. Co-UPDI or UPDI suspension, was dropped on two sides of the hydrophilic carbon paper ($1.0 \text{ cm}^2 \times 1.0 \text{ cm}$) as the working electrode used after drying at room temperatures.

2.7. Electrochemical oxygen evolution reaction (OER) test

The preparation process of the working electrode during the OER test is as follows: 5 mg of sample was firstly dispersed in 1.0 mL of aqueous solution by ultrasound to form a uniform suspension. Then $100 \mu\text{L}$ of suspension was dropped on glassy carbon electrode with the diameter of 5 mm and dried as the working electrode. As comparison, the electrocatalytic activity of clean UPDI and Co-UPDI for OER was also measured.

3. Result and discussion

3.1. Morphology and structure characterization

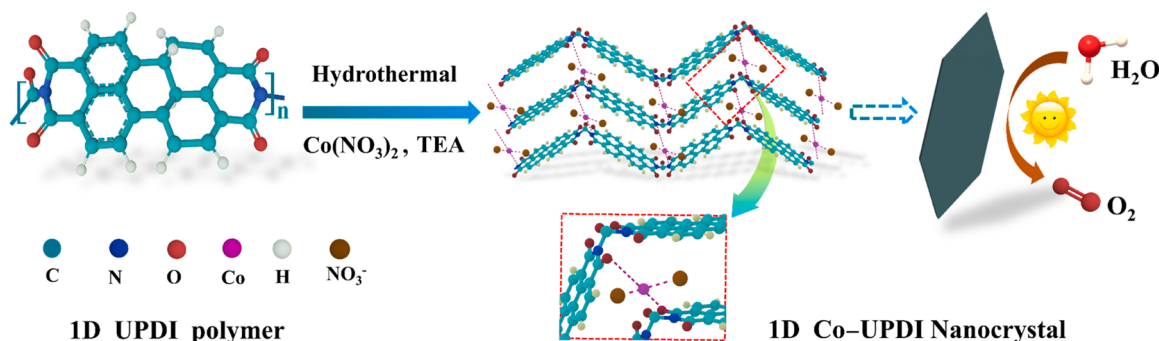
Basing on the reported UPDI polymer [31], the composite of UPDI molecular line and $\text{Co}(\text{NO}_3)_2$ molecules were tried preparing through the hydrothermal reaction at 120°C for 3 days, as illustrated in Scheme 1. The detailed process can be seen in Experimental section. The as-obtained sample was firstly characterized by scanning electron microscopy (SEM), transmission electron microscopy (TEM), selected area electron diffraction (SAED), element analysis (EA), X-ray photoelectron spectroscopy (XPS), X-ray diffraction pattern (XRD) and Fourier transform infrared Spectroscopy (FT-IR). The SEM images in Fig. 1a and Fig. S1 show the UPDI sample contains many 1D NRs with the average width of $\sim 200 \text{ nm}$ and length of $< 1 \mu\text{m}$. The inset reveals that its section is nearly square. After $\text{Co}(\text{NO}_3)_2$ was added, Fig. 1b and Fig. S2 display that a large amount of 1D nanostructure can be synthesized,

similar to UPDI sample. However, they are smaller and more regular 1D NRs with the average width of $\sim 100 \text{ nm}$ and the length of $\sim 500 \text{ nm}$. The inset in Fig. 1b reveals that its section should be rectangular, and its end is regular and surround by smooth crystal facets. The clear and periodically arranged SAED points in Fig. 1c prove that the as-prepared 1D nanostructure should be single crystal. The element mapping (Fig. 1d) indicates the existence of C, N, O and Co atoms, which are in accord with the XPS spectra in Fig. 1e. They are uniformly distributed in as-synthesized 1D sample. The differences of nanostructures in size, cross section and component with UPDI NRs imply the successful synthesis of 1D Co-UPDI nanocrystals.

To explore the crystal structure of Co-UPDI NRs, the XRD patterns and FT-IR spectra of UPDI and Co-UPDI NRs were measured and analyzed. In Fig. 1f (Bottom), the appearance of XRD peaks suggests that 1D UPDI NRs should be also crystal. The XRD peak at 27° (P2) results from the $\pi-\pi$ packing of perylene moiety with a typical d-spacing of $3.34-3.55 \text{ \AA}$ [33]. In XRD pattern of Co-UPDI sample (Top), there are three new peaks at 6.2° , 19.1° and 22° . Meanwhile, most of UPDI strong peaks, such as P1 and P2 peaks, still exist in the XRD pattern of Co-UPDI sample. It means that Co-UPDI should be a typical intercalated compound of UPDI crystal [34], in which $\text{Co}(\text{NO}_3)_2$ molecules may be orderly intercalated into the array of UPDI molecule lines [23]. In addition, the inset in Fig. 1f displays the P1 and P2 peaks shift to a higher angle and their intensity ratio of P2 to P1 increases, strongly indicating the closer $\pi-\pi$ stacking of PDI moiety in Co-UPDI than UPDI crystals. When FT-IR spectra of UPDI and Co-UPDI sample in Fig. 1g were compared, the four new peaks at 1549 , 1079 , 773 and 610 cm^{-1} can be clearly observed. They can be assigned to the antisymmetric stretching vibration, symmetric stretching vibration, out-of-plane bending vibration and in-plane bending vibration of $-\text{NO}_3^-$ anion, respectively [35]. The above experimental results clearly confirm that UPDI and $\text{Co}(\text{NO}_3)_2$ molecules have been successfully recombined into 1D Co-UPDI nanocrystals, in which $\text{Co}(\text{NO}_3)_2$ molecules should be embedded among UPDI molecule lines owing to the existence of certain strong interaction between $\text{Co}(\text{NO}_3)_2$ and UPDI. Consequently, the new XRD peak with bigger d-spacing generate at 6.2° . Meanwhile, the growth of some crystal facets should be suppressed, leading to a lower thickness of Co-UPDI NRs than UPDI ones.

3.2. POE performance

In view of the excellent POE activity of UPDI as reported [23], the photocatalytic activity of $\text{Co}(\text{NO}_3)_2$ -intercalated UPDI was investigated. In a typical process of photocatalytic water splitting to oxygen under visible light, 10 mg Co-UPDI or UPDI NRs as photocatalysts were firstly dispersed into 100 mL water to form the aqueous colloid system, including 5.0 mM AgNO_3 as electron acceptor. The detailed POE test can be found in Experimental section. In Fig. 2a, the POE rate of UPDI and Co-UPDI are summarized every 20 min . The Co-UPDI NRs exhibit an optimal POE rate of $7992.3 \mu\text{mol h}^{-1}\text{g}^{-1}$, which is about 13 times more



Scheme 1. The schematic diagram of synthesis process of 1D Co-UPDI nanocrystals.

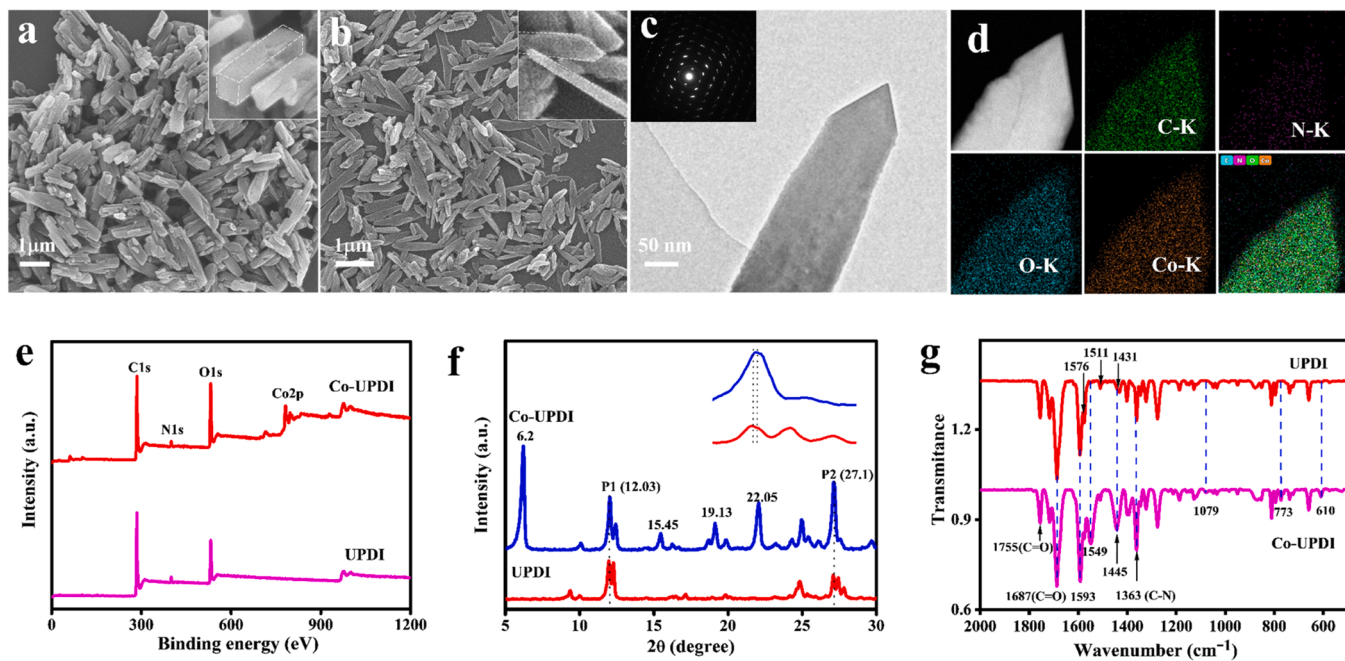


Fig. 1. SEM images of (a) UPDI and (b) Co-UPDI NRs, (c) TEM and SAED pattern, (d) HAADF-STEM and the elemental mapping images of C, N, O and Co atoms in Co-UPDI NRs, (e) XPS full spectra, (f) XRD patterns and (g) FT-IR spectra of UPDI and Co-UPDI NRs.

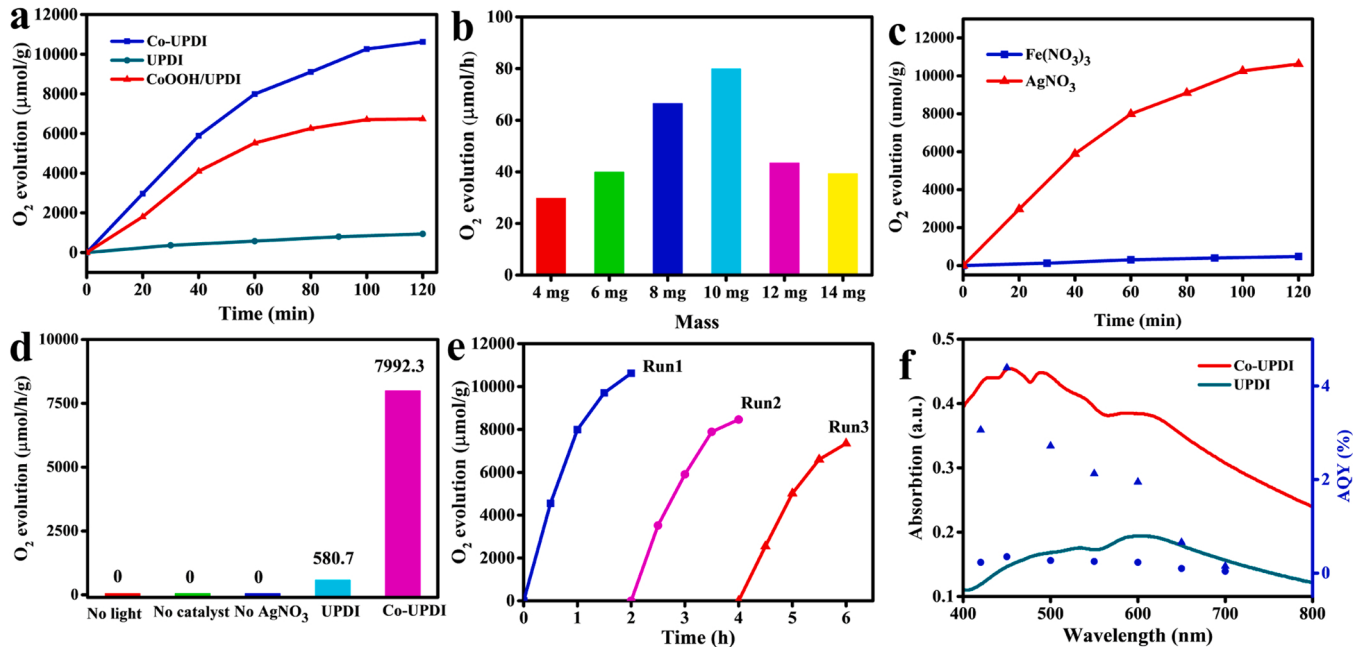


Fig. 2. (a) Time course of POE in 100 mL colloid system including 10 mg Co-UPDI, UPDI NRs or UPDI/CoOOH as catalyst and 5.0 mM AgNO₃ as sacrificial agent (pH = 4.8, $\lambda > 420$ nm, 20 °C). (b) The change of POE rate with the dosage of Co-UPDI NRs. (c-d) Effect of test condition on POE activity. (e) POE cycle experiments for 6 h. (f) AQY at different wavelengths and UV-vis absorption spectrum of UPDI and Co-UPDI NRs.

than UPDI (580.7 $\mu\text{mol h}^{-1}\text{g}^{-1}$). Here, the decrease of POE activity after one hour may be due to the consumption of AgNO₃ and generation of more silver nanoparticles on the surface of active sites. As compared to reported POE rate when AgNO₃ was used as sacrificial agent, the aqueous colloid system of Co-UPDI NRs also achieved the best POE activity (see Table S1). In addition, the effect of catalyst dosage on the POE rate was studied when the light absorption and scattering of nanomaterial were taken into account. The experimental results in Fig. 2b imply that 10 mg dosage should be optimal, and more or less catalyst is not good for POE process. Fig. 2c illustrates that Co-UPDI

NRs exhibit better POE activity in the presence of AgNO₃ rather than Fe (NO₃)₃ as sacrificial agent. It may be attributed to stronger electrophilic ability of Ag⁺ than Fe³⁺ ions and the reversible reaction between Fe³⁺ and Fe²⁺ ions [36]. In order to further verify the activity of Co-UPDI NRs as photocatalyst, the different tests were carried out under the conditions of no catalysts, no light and/or no sacrificial agents (see Fig. 2d). Obviously, Co-UPDI NRs exhibit the high catalytic activity only when light and AgNO₃ exist. The photostability of Co-UPDI is evaluated through three cycle tests under visible light irradiation, as shown in Fig. 2e. During the cycle tests, the Co-UPDI NRs was collected,

and then was washed with dilute nitric acid after a cycle, finally reused as photocatalyst for the next cycle. In the 2nd and 3rd tests, the POE performance slightly decreases due to the unavoidable loss of Co-UPDI NRs through the centrifugation of the previous reaction system. In addition, the AQY data of UPDI and Co-UPDI NRs at the wavelength of 420, 450, 500, 550, 600, 650 and 700 nm were also measured in aqueous phase. Fig. 2f, Table S2 and Table S3 display that the AQY of Co-UPDI is higher than UPDI (4.39 % vs. 0.35 %), indicating that Co-UPDI should have better ability of photocatalytic water oxidation.

After POE test, the catalyst was separated and characterized through XRD, XPS, SAED and TEM to further evaluate its stability and durability. As shown in Fig. 3, the structure and morphology of Co-UPDI NRs almost are kept unchanged. The XPS spectra in Fig. 3a and Fig. S3 confirm that the surface components of C, N, O and Co atoms still exist in Co-UPDI NRs. The XRD and SAED patterns in Fig. 3b, c reveal that the crystal structure of Co-UPDI NRs is also unbroken. However, the XRD peak in Fig. 3a at 6.2° becomes weaker with the decrease of Co content and the increase of Ag element, as compared with those of initial Co-UPDI NRs (see Fig. 1e and Fig. 3b). Meanwhile, the XPS peaks of C1s and N1s after reaction slightly shift in Fig. S3. Interestingly, the high-resolution TEM image (HRTEM) image in Fig. 3d uncovers the formation of CoOOH nanoparticles labeled in the red region (Fig. 3e), which has been proved to have an excellent catalytic activity for OER [37]. In addition, the unique twin crystal of Ag nanoparticles can be also seen in the yellow area in Fig. 3e, as shown in Fig. 3f. The above phenomena indicate that the surface $\text{Co}(\text{NO}_3)_2$ molecules may partially escaped from the crystal lattice of Co-UPDI crystal, and then form CoOOH nanoparticles as the OER active site enhancing interfacial reaction during POE test.

To further evaluate the effect of CoOOH as cocatalyst on POE activity, the CoOOH/UPDI composite was also synthesized through hydrothermal and in-situ oxidation methods. Here, the same amount of UPDI and $\text{Co}(\text{NO}_3)_2$ was used so that all of $\text{Co}(\text{NO}_3)_2$ molecules may

been transformed into CoOOH nanoparticles, as compared with the synthesis of Co-UPDI NRs. The detailed process can be found in Experimental Section 2.4. Fig. S4 shows the four typical peaks at 20.2° , 37.01° , 38.93° and 65.4° . They are consistent with the standard PDF card of CoOOH crystal (PDF No. #73-1213) [32], and may be indexed to (003), (101), (012) and (113) facets, respectively. In XRD pattern of CoOOH/UPDI sample, the peaks of UPDI and CoOOH are kept, implying the successful synthesis of CoOOH/UPDI composite. In addition, no obvious sign of Co-UPDI peaks, especially at 6.2° , can be observed, as compared with Fig. 1f. The SEM image in Fig. S5 displays the formation of a large amount of nanoparticle with the average size of < 10 nm. In our experiment, these nanoparticles may in-situ form on the surface of UPDI NRs, as shown in Fig. S6. The lattice space of 0.24 nm corresponding to the (101) facet of CoOOH crystal can be seen through HRTEM in Fig. S7 (see inset), further confirming the formation of CoOOH/UPDI composite. Under the same condition, the POE activity of CoOOH/UPDI composite as photocatalyst was also measured with AgNO_3 as sacrificial agent (see Fig. 2a). Indeed, the CoOOH/UPDI composite exhibits higher activity than UPDI NRs. Although more CoOOH nanoparticles exist in the CoOOH/UPDI composite than Co-UPDI NRs obtained after photocatalytic reaction, its activity is weaker than that of Co-UPDI NRs, indicating that the intercalation of $\text{Co}(\text{NO}_3)_2$ molecules into UPDI NRs plays the key role in the POE performance of Co-UPDI NRs.

3.3. POE process and analysis

To gain further insight into the above POE process, the light absorption, the generation and transfer of photoinduced electron/hole and interfacial reaction were studied when UPDI and Co-UPDI NRs were used as photocatalyst, respectively. As shown in Fig. 4a, UPDI and Co-UPDI solution in DMSO has the similar absorption characteristics to perylene [38]. The four characteristic absorption peaks at 415, 457, 486 and 523 nm derive from perylene stretching modes of 0 – 3, 0 – 2,

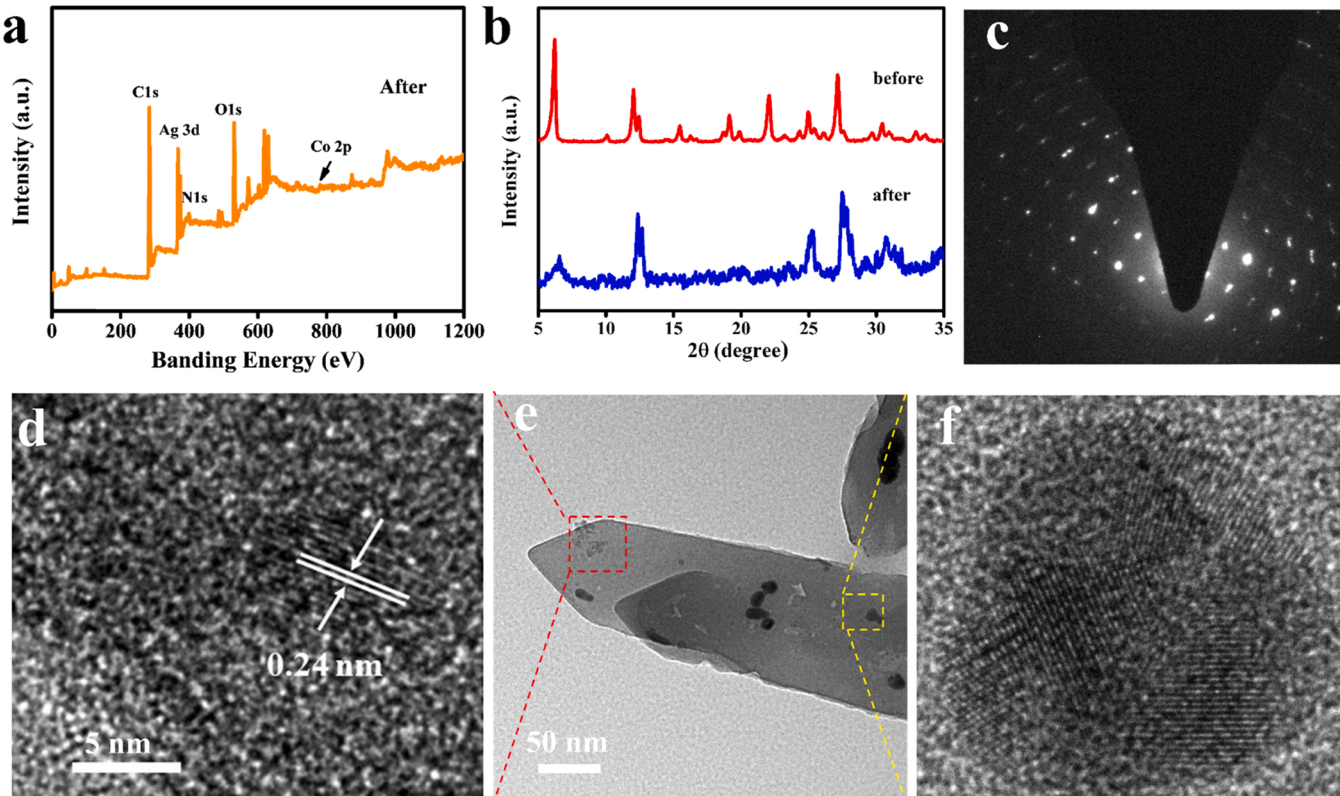


Fig. 3. (a) XPS spectra and (b) XRD patterns of Co-UPDI NRs before/after POE test. (c) TEM image and SAED pattern, and (d-f) HRTEM images at red and yellow regions after POE test.

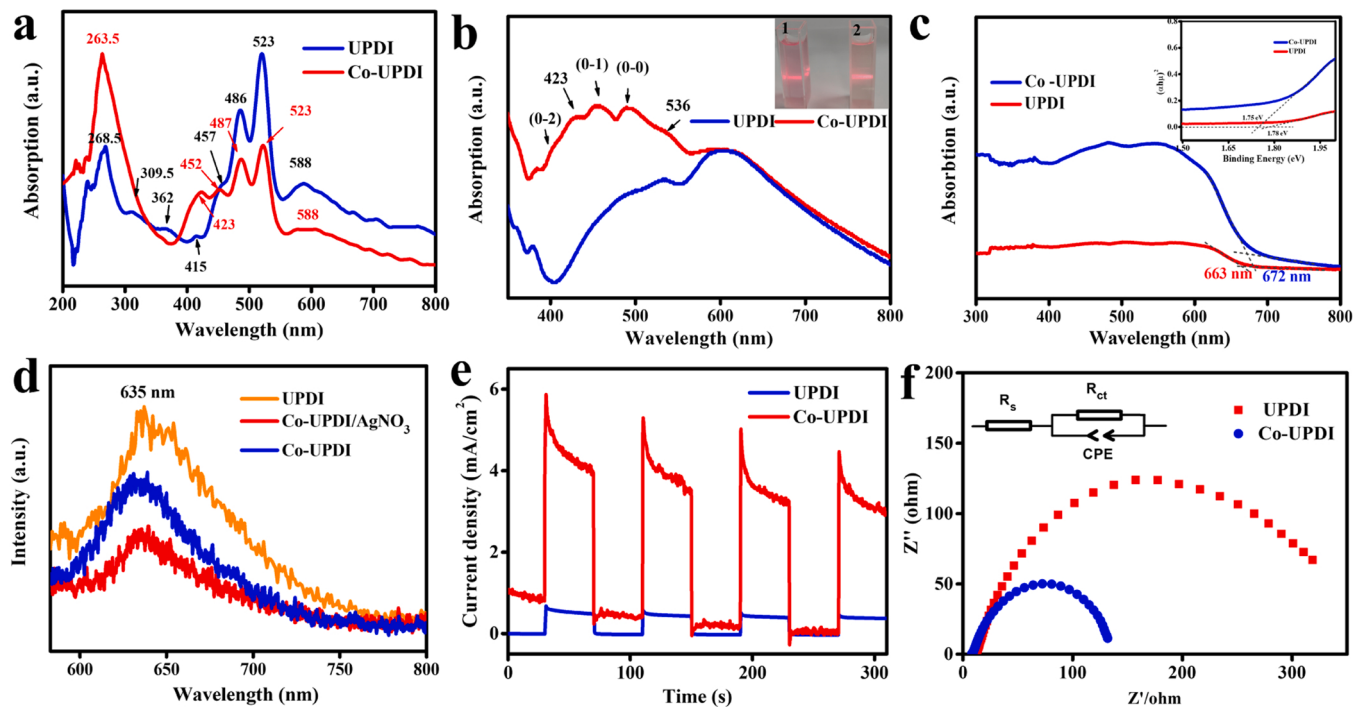


Fig. 4. UV-vis absorption spectra in (a) DMSO solution and (b) aqueous colloid system, (c) DRS spectra and Band gap, (d) PL spectra ($\lambda_{\text{Ex}} = 450$ nm), (e) TPR and (f) EIS curves of UPDI and Co-UPDI NRs.

0–1 and 0–0 when coupled to the $\pi\rightarrow\pi^*$ electronic transition. The peaks at 575 and 588 nm should be from the charge transfer (CT) from perylene moiety to $-\text{C}=\text{O}$ and $-\text{urea}$ groups. In addition, the peaks of perylene anion can be observed between 650 and 800 nm [39]. When the absorption spectrum of UPDI is compared with that of Co-UPDI in DMSO, the most obvious change is the decrease of absorption intensity of Co-UPDI between 400 and 800 nm, strongly indicating the reduction or intermolecular transfer of π electron from UPDI to $\text{Co}(\text{NO}_3)_2$ molecules. In addition, a new peak generates at 423 nm. It should result from the interaction between UPDI and $\text{Co}(\text{NO}_3)_2$, resulting in the formation of new conjugated structure similar to that of Co-N_4 conjugated ring [40]. The intensity of 0–3 absorption peak at 415 nm also becomes stronger in Co-UPDI than UPDI, which can be attributed to the enhancement of bay area vibration mode [41]. That is, the stretching along short axis direction and the contraction along long axis direction of UPDI molecule line are enhanced in Co-UPDI.

After 10 mg UPDI and/or Co-UPDI NRs were dispersed into 100 mL water to form colloidal system, the obvious Tyndall effect can be observed from inset in Fig. 4b, indicating them good water dispersibility. However, their UV-Vis spectra in aqueous dispersing system have also obvious differences, as compared with those in DMSO solution. 1) The blue-shift can be found, e.g. the 0–0 peak appears at 493 nm rather than 523 nm. Meanwhile, the relative position of four typical peaks of 0–0, 0–1, 0–2 and 0–3 from perylene moiety changes. 2) The intramolecular CT state from perylene to substituent groups at > 580 nm enhances, especially in UPDI NRs due to bigger size than Co-UPDI (see Fig. 1). 3) The 0–0 peak at 493 nm weakens, even is lower than those of 0–1 peak in Co-UPDI. It is a typical signal of the formation of perylene H-type aggregate at 536 nm [42]. The higher intensity ratio of 0–1 to 0–0 peaks also mean closer stacking of perylene moiety in Co-UPDI than UPDI, resulting in the more efficient intermolecular CT [23]. This is the reason why the absorption intensity between 400 and 580 nm is stronger in Co-UPDI NRs than UPDI NRs. Actually, the light absorption Co-UPDI NRs is also better to match sunlight spectrum [23]. 4) The absorption peak at 423 nm becomes stronger in Co-UPDI NRs than solution, meaning the possible existence of more Co–N conjugated structure and

heterojunction sites between UPDI molecular line and $\text{Co}(\text{NO}_3)_2$ molecules. According to the solid-state ultraviolet diffuse reflection spectrum (DRS), the band gap of UPDI and Co-UPDI NRs can be obtained. As shown in Fig. 4c, the DRS of Co-UPDI NRs with the boundary at 672 nm has the wider visible-light adsorption than that of UPDI at 663 nm. Their band gaps can be derived from the intercept of the tangent to the plot of $(\alpha h\nu)^2$ versus $h\nu$ by Tauc method in inset [43]. The results uncover that Co-UPDI NRs have a narrower band gap (1.75 eV) than UPDI (1.78 eV). The valence band spectroscopy (VB XPS) spectra in Fig. S8 display that the binding energy of Co-UPDI (1.67 eV) is high than that of UPDI (1.52 eV), implying the π electron transfer from UPDI to $\text{Co}(\text{NO}_3)_2$.

In Fig. 4d, the photoluminescence (PL) spectra of Co-UPDI (red line) and UPDI (blue line) upon the excitation wavelength of 450 nm show the decrease of fluorescence intensity at 635 nm from UPDI, Co-UPDI to Co-UPDI/ AgNO_3 in aqueous colloid system. The phenomenon explains why the efficiency of photoelectric conversion of Co-UPDI NRs is better than UPDI. To directly understand the behavior of photoinduced carriers, the transient photocurrent response (TPR) of UPDI and Co-UPDI NRs were measured, as shown in Fig. 4e. It can be found that the photocurrent of Co-UPDI NRs is more an order of magnitude higher than that of UPDI NRs. Theoretically, this should be the key reason why the POE activity of Co-UPDI is better. Here, the fast decreases of initial photocurrent of Co-UPDI may be attributed to the part escape of $\text{Co}(\text{NO}_3)_2$ molecules from Co-UPDI NRs, and then was transformed into CoOOH on the surface of Co-UPDI NRs under light irradiation (see Fig. 3). Consequently, the transportation of photogenerated carriers is hindered, resulting in easy recombination of photogenerated electrons and holes [44]. Meanwhile, the electrochemical impedance spectroscopy (EIS) was also measured. As illustrated in the Fig. 4f, the internal resistance of Co-UPDI is smaller than that of UPDI, suggesting that the easier electron transfer in Co-UPDI NRs. Furthermore, their electrocatalytic activity for OER was investigated to explore the ability of interfacial reaction. Fig. S9 manifests that Co-UPDI NRs have a lower overpotential than UPDI NRs, especially after CoOOH nanoparticles form during POE. The overpotential difference is more obvious at low photocurrent density. On the basis of the above analysis, we can make a

conclusion that after $\text{Co}(\text{NO}_3)_2$ molecules were intercalated into 1D UPDI nanocrystals to form the intermolecular heterojunction, not only the photoelectric conversion efficiency is improved, but also the activity of interfacial OER is enhanced.

3.4. Structure and components analysis

To further study the difference of UPDI and Co-UPDI in crystal structure and components, which plays an important role in POE performance, the corresponding XPS and FT-IR spectra were carefully analyzed besides the UV-Vis spectra. Here, high-resolution XPS spectra of N 1s, C 1s, O 1s and Co 2p are divided to investigate the changes of various moieties. As reported [23], the N 1s XPS spectrum of UPDI has only a peak of N-C bond at 400.3 eV. For the N 1s XPS spectrum of Co-UPDI in Fig. 5a, two peaks at 399.9 eV and 401.2 eV may be assigned to the N-C and NO_3^- [35]. Obviously, the binding energy of N 1s in N-C bond decreases by 0.4 eV, as compared with that in UPDI. The C 1s spectrum of UPDI in Fig. 5b includes three typical peaks of C=O, C-N and C-C moieties at 288.3, 285.3 and 284.8 eV. Correspondingly, the binding energy of C 1s in C-N bond increase to 286.0 eV in Co-UPDI. The change of C, N binding energy proves the C-N bond length shorter and bond energy higher in Co-UPDI than UPDI. For the O 1s spectrum of UPDI in Fig. 5c, two peaks at 533.4 and 531.4 eV can be considered as bound water and C=O bond [45]. The new peak of O 1s spectrum at 532.6 eV in Co-UPDI belongs to the NO_3^- ion. Two peaks of Co 2p at 796.9 and 780.9 eV in Fig. 5d together with their satellite peaks are from the electron transition of $2p_{1/2}$ and $2p_{3/2}$ orbits of Co^{2+} [46].

In the FT-IR spectrum of UPDI in Fig. 1g (TOP), two peaks at 1687 and 1755 cm^{-1} can be assigned to in-plane(asymmetric) and out-of-plane (symmetric) stretching vibration of C=O bond [27]. The peaks at 1593, 1576, 1511 and 1431 cm^{-1} belong to the breathing vibration of aromatic ring when connected with C=O group [47]. The peak at 1361 cm^{-1} can be attributed to the stretching vibration of C-N bond [24]. After the recombination of UPDI line with $\text{Co}(\text{NO}_3)_2$ molecules into Co-UPDI, there are two obvious changes besides the appearance

four typical peaks of NO_3^- ion [48]. 1) The vibration of aromatic ring enhances, as compared with that of C=O bond. Especially, the peak at 1431 cm^{-1} blue-shifts to 1445 cm^{-1} and obviously heightens. It strongly suggests that the planarity or rigidity of aromatic ring should be enhanced, agreeing with the absorption enhancement of H-type aggregates and the decrease of its d-spacing. 2) The vibration of C-N bond at 1361 cm^{-1} becomes stronger, meaning that the rigidity of C-N bond enhances. It is accordant with the XPS results. The above phenomena actually confirm that the rigidity of whole UPDI molecule line actually become better after the $\text{Co}(\text{NO}_3)_2$ molecules were intercalated into UPDI crystal. Combining the difference of UPDI and Co-UPDI in UV-Vis absorption and energy level, these changes in XPS and FT-IR spectra may be attributed to the CT from N atom in UPDI to Co atom in $\text{Co}(\text{NO}_3)_2$ due to the possible coordination interaction. At the moment, the lost electrons on N atom may be compensated from adjacent C atoms, and then Co-N-C structure forms in Co-UPDI crystal. Taking planar four-coordination capability of Co^{2+} into account, a Co atom may link with two NO_3^- ions and two N atoms from adjacent molecule lines, as illustrated in Scheme 1. Consequently, a planar and symmetrical structure generates, accompanying the appearance of a new absorption peak at 423 nm. The connection of PDI with Co conjugated ring through N-C bond should be the nature of Z-scheme heterojunction between UPDI line and $\text{Co}(\text{NO}_3)_2$ molecules in Co-UPDI. On the basing of analysis for Co-UPDI structure, it may be believed that the heterojunction formation and the rigidity enhancement of UPDI molecule line in Co-UPDI crystals should be two main structure factors why Co-UPDI NRs may exhibit better POE activity, especially more excellent ability of photoelectric conversion than UPDI NRs. In addition, there may be $\text{Co}(\text{NO}_3)_2$ molecules on Co-UPDI NRs on Co-UPDI NRs, which is helpful to generate CoOOH as cocatalyst in initial photocatalytic reaction.

3.5. Photoelectric mechanism

In order to understand the structure effect of UPDI and Co-UPDI NRs on the photoelectric conversion, the femtosecond transient absorption

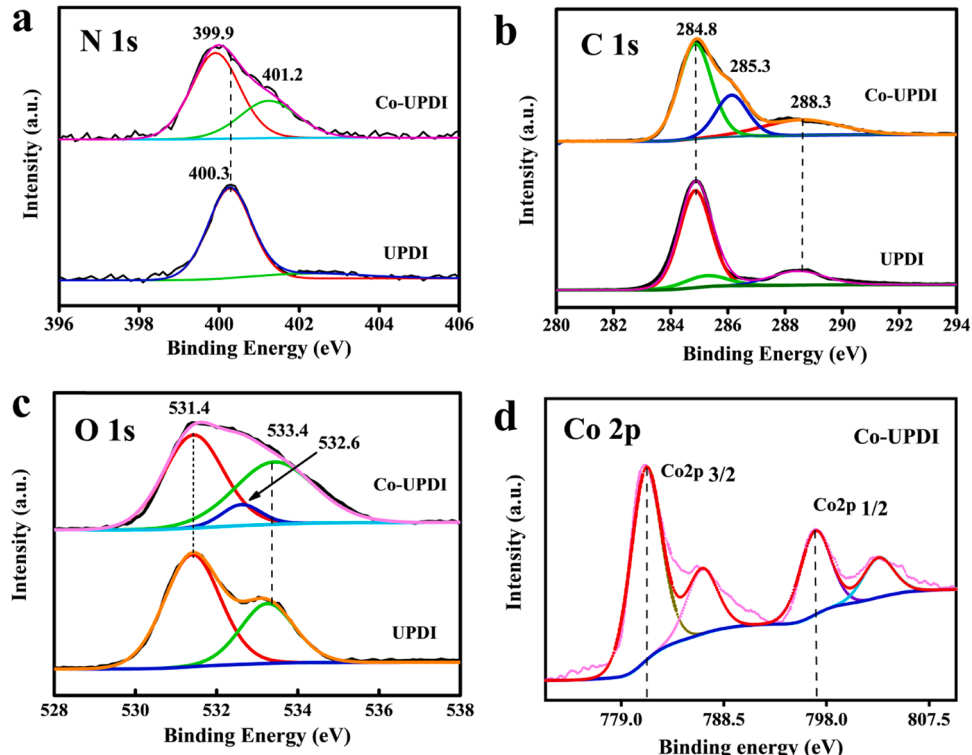


Fig. 5. High-resolution XPS spectra of (a) N 1s, (b) C 1s, (c) O 1s and (d) Co 2p in UPDI and Co-UPDI NRs.

(fsTA) spectroscopy ($\lambda_{\text{ex}} = 360$ nm, 4.0 mJ/Pulse) was measured to investigate their difference of photoinduced carriers. In the fsTA spectra of UDPI NRs (Fig. 6a-b), the negative ground-state bleaching (GB) peaks can be easily found at 400–536 nm, 580–610 nm due to the light absorption of PDI moiety, H-type aggregate and intramolecular electron transition, as shown in Fig. 4. Meanwhile, the strong negative stimulated emission (SE) peak at 640 nm appears (see Fig. 4d), which is accompanied with the weak positive excited state absorption (ESA) peaks at 513 and 560 nm assigned to the electron transition (ET) of $S_1 \rightarrow S_N$ in and between PDI moiety. It means that the exciton formation of intermolecular CT state (PDI⁺•PDI⁻) and/or polarized exciton (PDI⁺•PDI⁻)*. Co-UPDI and UPDI NRs have similar UV-visible absorption and PL spectra, however, their fsTA spectra have a considerable differences. For the fsTA spectra of Co-UPDI in Fig. 6c-d, the corresponding GB and SE peaks become weaker, on the contrary, the ESA peaks from 400 to 700 nm notably become stronger. It stands for the generation of more polarized excitons with higher energy in Co-UPDI rather than low-energy exciton from the ET of $S_0 \rightarrow S_1$ in UPDI. This should be a key reason why higher photocurrent generates in Co-UPDI NRs.

As we know, the efficiency of photoelectrical conversion depends on the generation, transportation and recombination of photoinduced excitons. To achieve high efficiency of photoelectric conversion, the long-distance transportation and separation of more excitons with long lifetime is a key after the faster generation. According to the occurrence order of fsTA peaks with the detection time in Fig. 6, it can be observed

that upon light irritation, the generation and transport of carriers in both UPDI and Co-UPDI NRs should undergo a same path from PDI moiety, PDI aggregate to urea moiety (C–N) in UPDI molecule line. The fsTA spectra in Fig. 6a, c show that the photoinduced electron firstly generates at perylene moiety within 10.0 fs. For the intermolecular and intramolecular CT state excitons, the subsequent fast generation and transportation in PDI aggregate and slow recombination in UPDI molecule line should be the key factors influencing the photoelectric conversion. The analysis of corresponding kinetics reveals that the lifetimes of formation and deexcitation of (PDI⁺•PDI⁻)* polarized exciton at 560 nm, which derives from the absorption of aggregate (PDI•PDI) at 536 nm, are ~23.04 ps in UPDI NRs and ~10.79 ps in Co-UPDI NRs, as shown in Fig. 6e. After the carrier transferred from PDI to urea moiety (C–N site), it can be seen in Fig. 6f that the charge recombination lifetimes (τ_{CR}) at 640 nm are 2.3 ps in UPDI and 100.1 ps in Co-UPDI, respectively. Here, it must be noticed that the formation of SE peak at 640 nm in UPDI NRs means the generation and deexcitation of intramolecular CT exciton at C–N site. The formation of ESA peak at 640 nm in Co-UPDI NRs should be the generation and absorption of intermolecular CT state exciton from C–N site to Co atoms. In other words, the CT excitons disappear at C–N site in UPDI due to the possible relaxation oscillation of flexible C–N single bond, however continuously transport to Co(NO₃)₂ molecule in Co-UPDI NRs. In general, the faster CT in PDI aggregate and longer τ_{CR} should be another key reason why the photoelectric property of Co-UPDI NRs is better than UPDI NRs.

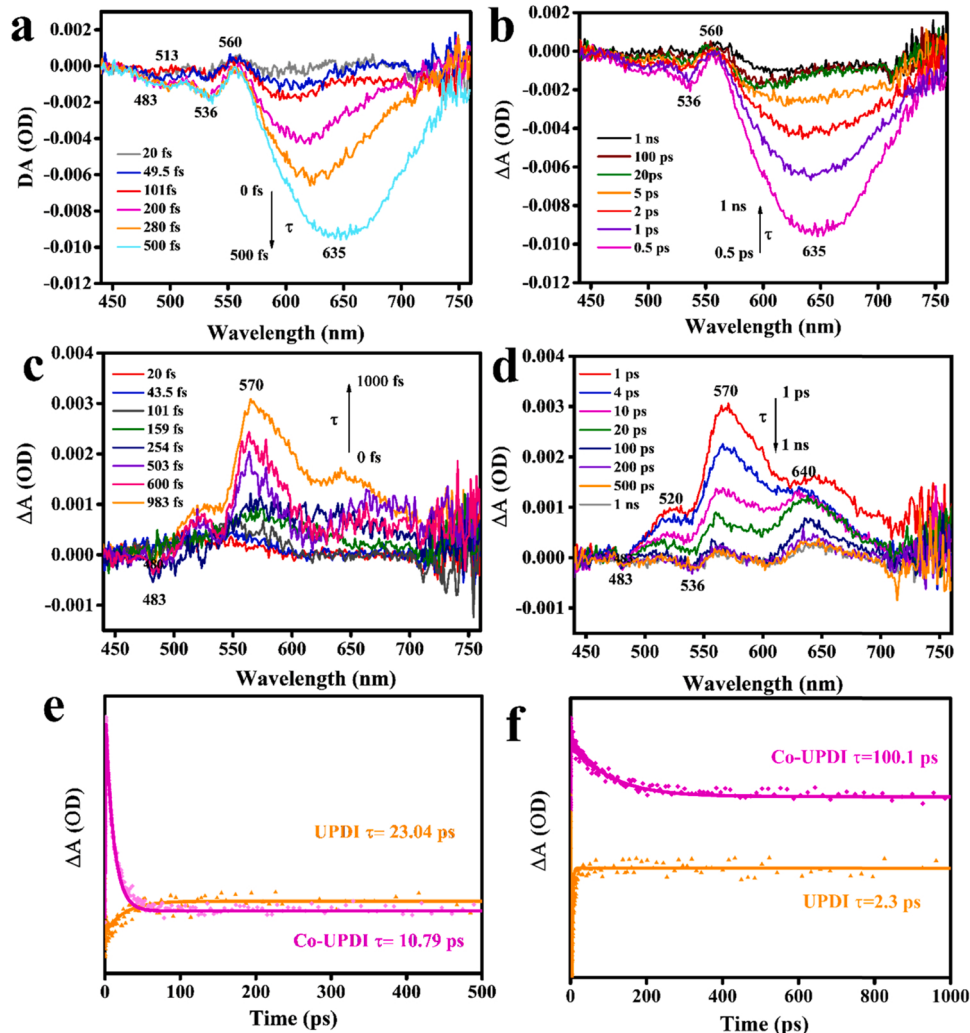
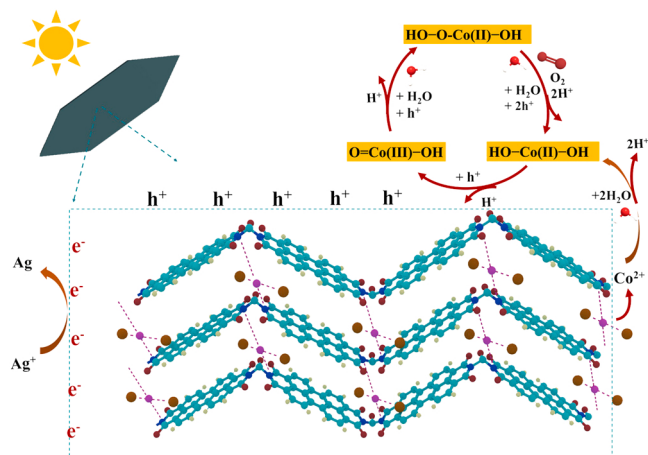


Fig. 6. The fsTA spectra of (a-b) UPDI and (c-d) Co-UPDI, and fsTA kinetics lifetimes of UPDI and Co-UPDI NRs at (e) 560 nm and (f) 640 nm.



Scheme 2. The structure and POE mechanism of Co-UPDI NRs with AgNO_3 as electron acceptor.

These also perfectly reflect the effect of closer stacking of PDI moiety and the shorter bond length of C–N on photocurrent after $\text{Co}(\text{NO}_3)_2$ molecules were intercalated into UPDI crystal.

On the basis of our experimental results and corresponding analysis, the possible structure of Co-UPDI single crystal and the corresponding POE process may be speculated, as illustrated in **Scheme 2**. Under a suitable hydrothermal condition, the $\text{Co}(\text{NO}_3)_2$ molecules may be intercalated into the 1D nanocrystal of UPDI molecule line to form 1D Co-UPDI nanocomposite owing to the coordination interaction between N and Co atoms. A new conjugated structure should generate owing to the planar four coordination of Co(II) atom with two NO_3^- ions and two N atoms from two adjacent UPDI molecule lines, and periodically arrange among UPDI molecule lines. The new crystal facets form when those of UPDI arrangement are almost kept. Meanwhile, the intercalation of $\text{Co}(\text{NO}_3)_2$ molecules leads to the enhancement the rigidity of UPDI molecule line, involving the planarity improvement of PDI moiety and the shortening of C–N bond length. Upon the light irritation, 1D nanocrystals of Co-UPDI have wider and more suitable absorption for solar light than UPDI. More importantly, the photo-generated electron in perylene chromophore can be quickly and easily transported to crystal surface through the intermolecular and intramolecular CT from PDI, urea moiety to $\text{Co}(\text{NO}_3)_2$ molecules. It avoids the fast exciton annihilation due to the relaxation oscillation of flexible C–N bond. During the POE process in aqueous colloid system of Co-UPDI NRs with AgNO_3 as electron acceptor, the partial dissociation of $\text{Co}(\text{NO}_3)_2$ molecules from Co-UPDI surface may hydrolyze, and then be oxidized by the photoinduced holes to the highly-efficient active CoOOH nanoparticles for the interfacial OER reaction. AgNO_3 is reduced to silver nanoparticles. The water oxidation on the surface of CoOOH under weak acid condition usually undergoes the three steps [27]. 1) The OH^- ions are chemically adsorbed by electrophilic Co(III), and the OOH^* intermediate forms. 2) The oxygen generates due to the fast decomposition of side-on unstable superoxide species to HO-Co(II)-OH . 3) The CoOOH generates again owing to the oxidation of HO-Co(II)-OH by a photoinduced hole.

4. Conclusion

In summary, we have successfully synthesized the 1D nanocrystals of cobalt-intercalated UPDI composite through a simple hydrothermal method to promote the POE activity of UPDI with intrinsic strong built-in electric field. Upon visible light irritation ($\lambda > 420 \text{ nm}$), Co-UPDI NRs exhibited more an order of magnitude of POE rate of UPDI NRs (8.00 vs. 0.58 $\text{mmol h}^{-1} \text{g}^{-1}$) in 100 mL acid aqueous dispersed system including 5.0 mM AgNO_3 as electron acceptor. The AQY of 4.39% may

be obtained at 450 nm. The investigation in the light absorption, photoelectric property and electrocatalytic OER displayed that the high POE performance of Co-UPDI should result from the improvement of photoelectric conversion efficiency and in-situ formation of CoOOH as cocatalyst. A series of characterizations confirmed the formation of Z-scheme heterojunction due to the coordination interaction of Co with N atoms between UPDI and $\text{Co}(\text{NO}_3)_2$, and the rigidity enhancement of UPDI molecule line, especially at flexible C–N site in Co-UPDI NRs. As a result, the faster generation and transportation of photoinduced carriers with the longer lifetime may be achieved in Co-UPDI than UPDI NRs. This work provides a promising strategy for PDI-based nanocrystals as catalyst to enhance the photocatalytic water oxidation under solar visible light.

CRediT authorship contribution statement

Aihui Cao: Conceptualization, Methodology, Investigation, Data Curation, Writing – original draft. **Renfu Li:** Software, Data curation. **Xiao Xu:** Data curation, Formal analysis. **Weifeng Huang:** Visualization, Investigation. **Ying He:** Data curation, Investigation. **Junqiang Li:** Software, Validation. **Miao Sun:** Software, Data curation. **Xueyuan Chen:** Resources, Supervision. **Longtian Kang:** Conceptualization, Funding acquisition, Resources, Supervision, Writing – review & editing.

Declaration of Competing Interest

The authors declare that they have no known competing financial interests or personal relationships that could have appeared to influence the work reported in this paper.

Acknowledgements

This work was supported by the Fujian Science & Technology Innovation Laboratory for Optoelectronic Information of China (2021ZR124) and National Natural Science Foundation of China (21705150, 21473204).

Appendix A. Supporting information

Supplementary data associated with this article can be found in the online version at [doi:10.1016/j.apcatb.2022.121293](https://doi.org/10.1016/j.apcatb.2022.121293).

References

- [1] M.A. Ghausi, J. Xie, Q. Li, X. Wang, R. Yang, M. Wu, Y. Wang, L. Dai, CO_2 overall splitting by a bifunctional metal-free electrocatalyst, *Angew. Chem. Int. Ed.* 57 (2018) 13135–13139.
- [2] X. Liu, S. Inagaki, J. Gong, Heterogeneous molecular systems for photocatalytic CO_2 reduction with water oxidation, *Angew. Chem. Int. Ed.* 55 (2016) 14924–14950.
- [3] T. Takata, J. Jiang, Y. Sakata, M. Nakabayashi, N. Shibata, V. Nandal, K. Seki, T. Hisatomi, K. Domen, Photocatalytic water splitting with a quantum efficiency of almost unity, *Nature* 581 (2020) 411–414.
- [4] H. Lu, J. Tournet, K. Dastafkan, Y. Liu, Y.H. Ng, S.K. Karuturi, C. Zhao, Z. Yin, Noble-metal-free multicomponent nanointegration for sustainable energy conversion, *Chem. Rev.* 121 (2021) 10271–10366.
- [5] Q. Wang, K. Domen, Particulate photocatalysts for light-driven water splitting: mechanisms, challenges, and design strategies, *Chem. Rev.* 120 (2020) 919–985.
- [6] Y. Wang, T. He, Recent advances in and comprehensive consideration of the oxidation half reaction in photocatalytic CO_2 conversion, *J. Mater. Chem. A* 9 (2021) 87–110.
- [7] S. Chang, J. Yu, R. Wang, Q. Fu, X. Xu, LaTaON_2 mesoporous single crystals for efficient photocatalytic water oxidation and Z-scheme overall water splitting, *ACS Nano* 15 (2021) 18153–18162.
- [8] J.K.J.S. Hurst, In pursuit of water oxidation catalysts for solar fuel production, *Science* 328 (2010) 315–316.
- [9] S. Lin, H. Huang, T. Ma, Y. Zhang, Photocatalytic oxygen evolution from water splitting, *Adv. Sci.* 8 (2020), 2002458.
- [10] W.J. Ong, L.L. Tan, Y.H. Ng, S.T. Yong, S.P. Chai, Graphitic carbon nitride ($\text{g-C}_3\text{N}_4$)-based photocatalysts for artificial photosynthesis and environmental remediation: are we a step closer to achieving sustainability? *Chem. Rev.* 116 (2016) 7159–7329.

[11] J. Abdul Nasir, A. Munir, N. Ahmad, T.U. Haq, Z. Khan, Z. Rehman, Photocatalytic Z-scheme overall water splitting: recent advances in theory and experiments, *Adv. Mater.* (2021), e2105195.

[12] J. Low, C. Jiang, B. Cheng, S. Wageh, A.A. Al-Ghamdi, J. Yu, A review of direct Z-scheme photocatalysts, *Small Methods* 1 (2017).

[13] J. Feng, J. Bian, L. Bai, S. Xi, Y. Wang, C. Chen, L. Jing, Efficient wide-spectrum photocatalytic overall water splitting over ultrathin molecular nickel phthalocyanine/BiVO₄ Z-scheme heterojunctions without noble metals, *Appl. Catal. B: Environ.* 295 (2021) 12060.

[14] W. Zhang, W. Lai, R. Cao, Energy-related small molecule activation reactions: oxygen reduction and hydrogen and oxygen evolution reactions catalyzed by porphyrin- and corrole-based systems, *Chem. Rev.* 117 (2017) 3717–3797.

[15] F.P. Kinik, A. Ortega-Guerrero, D. Ongari, C.P. Ireland, B. Smit, Pyrene-based metal organic frameworks: from synthesis to applications, *Chem. Soc. Rev.* 50 (2021) 3143–3177.

[16] Y. Choi, D. Jeon, Y. Choi, J. Ryu, B.S. Kim, Self-assembled supramolecular hybrid of carbon nanodots and polyoxometalates for visible-light-driven water oxidation, *ACS Appl. Mater. Interfaces* 10 (2018) 13434–13441.

[17] J. Yang, B. Xiao, A. Tang, J. Li, X. Wang, E. Zhou, Aromatic-diimide-based n-type conjugated polymers for all-polymer solar cell applications, *Adv. Mater.* 31 (2019), e1804699.

[18] S. Chen, P. Slattum, C. Wang, L. Zang, Self-assembly of perylene imide molecules into 1D nanostructures: methods, morphologies, and applications, *Chem. Rev.* 115 (2015) 11967–11998.

[19] J. Wang, W. Shi, D. Liu, Z. Zhang, Y. Zhu, D. Wang, Supramolecular organic nanofibers with highly efficient and stable visible light photooxidation performance, *Appl. Catal. B: Environ.* 202 (2017) 289–297.

[20] S. Chen, C. Wang, B.R. Bunes, Y. Li, C. Wang, L. Zang, Enhancement of visible-light-driven photocatalytic H₂ evolution from water over g-C₃N₄ through combination with perylene diimide aggregates, *Appl. Catal. A* 498 (2015) 63–68.

[21] K.E. Brown, W.A. Salamant, L.E. Shoer, R.M. Young, M.R. Wasielewski, Direct observation of ultrafast excimer formation in covalent perylenediimide dimers using near-infrared transient absorption spectroscopy, *J. Phys. Chem. Lett.* 5 (2014) 2588–2593.

[22] J.T. Kirner, J.J. Stracke, B.A. Gregg, R.G. Finke, Visible-light-assisted photoelectrochemical water oxidation by thin films of a phosphonate-functionalized perylene diimide plus CoO_x cocatalyst, *ACS Appl. Mater. Interfaces* 6 (2014) 13367–13377.

[23] Z. Zhang, X. Chen, H. Zhang, W. Liu, W. Zhu, Y. Zhu, A highly crystalline perylene imide polymer with the robust built-in electric field for efficient photocatalytic water oxidation, *Adv. Mater.* 32 (2020), e1907746.

[24] J. Zhou, Y. Wang, Z. Cui, Y. Hu, X. Hao, Y. Wang, Z. Zou, Ultrathin conjugated polymer nanosheets as highly efficient photocatalyst for visible light driven oxygen activation, *Appl. Catal. B: Environ.* 277 (2020), 119228.

[25] J. Wang, D. Liu, Y. Zhu, S. Zhou, S. Guan, Supramolecular packing dominant photocatalytic oxidation and anticancer performance of PDI, *Appl. Catal. B: Environ.* 231 (2018) 251–261.

[26] L. Zeng, T. Liu, C. He, D. Shi, F. Zhang, C. Duan, Organized aggregation makes insoluble perylene diimide efficient for the reduction of aryl halides via consecutive visible light-induced electron-transfer processes, *J. Am. Chem. Soc.* 138 (2016) 3958–3961.

[27] Z. Zhong, R. Li, W. Lin, X. Xu, X. Tian, X. Li, X. Chen, L. Kang, One-dimensional nanocrystals of cobalt perylene diimide polymer with in-situ generated FeOOH for efficient photocatalytic water oxidation, *Appl. Catal. B: Environ.* 260 (2020), 118135.

[28] S. Siracusano, N. Van Dijk, E. Payne-Johnson, V. Baglio, A.S. Aricò, Nanosized IrO_x and IrRuO_x electrocatalysts for the O₂ evolution reaction in PEM water electrolyzers, *Appl. Catal. B: Environ.* 164 (2015) 488–495.

[29] X. Liu, J. Meng, J. Zhu, M. Huang, B. Wen, R. Guo, L. Mai, Comprehensive understandings into complete reconstruction of precatalysts: synthesis, applications, and characterizations, *Adv. Mater.* 33 (2021), e2007344.

[30] Z. Shuai, H. Geng, W. Xu, Y. Liao, J.M. Andre, From charge transport parameters to charge mobility in organic semiconductors through multiscale simulation, *Chem. Soc. Rev.* 43 (2014) 2662–2679.

[31] P. Sharma, D. Damien, K. Nagarajan, M.M. Shajumon, M. Hariharan, Perylene-polyimide-based organic electrode materials for rechargeable lithium batteries, *J. Phys. Chem. Lett.* 4 (2013) 3192–3197.

[32] J. Huang, Q. Shang, Y. Huang, F. Tang, Q. Zhang, Q. Liu, S. Jiang, F. Hu, W. Liu, Y. Luo, T. Yao, Y. Jiang, Z. Pan, Z. Sun, S. Wei, Oxyhydroxide nanosheets with highly efficient electron-hole pair separation for hydrogen evolution, *Angew. Chem. Int. Ed.* 55 (2016) 2137–2141.

[33] T. Cai, W. Zeng, Y. Liu, L. Wang, W. Dong, H. Chen, X. Xia, A promising inorganic-organic Z-scheme photocatalyst Ag₃PO₄/PDI supermolecule with enhanced photoactivity and photostability for environmental remediation, *Appl. Catal. B: Environ.* 263 (2020), 118327.

[34] P.-a Zong, Z. Mao, Y. Ou, T. Shi, Z. Wang, Q. Zhang, P. Zhang, C. Wan, Enhanced thermoelectric properties of binary CoSb₃ by embedding FeCl₃-intercalated graphene nanosheets, *J. Eur. Ceram. Soc.* 41 (2021) 6523–6530.

[35] J. Chen, X. Tao, C. Li, Y. Ma, L. Tao, D. Zheng, J. Zhu, H. Li, R. Li, Q. Yang, Synthesis of bipyridine-based covalent organic frameworks for visible-light-driven photocatalytic water oxidation, *Appl. Catal. B: Environ.* 262 (2020), 118271.

[36] Z. Wei, W. Wang, W. Li, X. Bai, J. Zhao, E.C.M. Tse, D.L. Phillips, Y. Zhu, Steering electron-hole migration pathways using oxygen vacancies in tungsten oxides to enhance their photocatalytic oxygen evolution performance, *Angew. Chem. Int. Ed.* 60 (2021) 8236–8242.

[37] Z.Y. Wang, L. Wang, S. Liu, G.R. Li, X.P. Gao, Conductive CoOOH as carbon-free sulfur immobilizer to fabricate sulfur-based composite for lithium-sulfur battery, *Adv. Funct. Mater.* 29 (2019), 1901051.

[38] Q. Bao, B.M. Goh, B. Yan, T. Yu, Z. Shen, K.P. Loh, Polarized emission and optical waveguide in crystalline perylene diimide microwires, *Adv. Mater.* 22 (2010) 3661–3666.

[39] X. Chen, J. Wang, Y. Chai, Z. Zhang, Y. Zhu, Efficient photocatalytic overall water splitting induced by the giant internal electric Field of a g-C₃N₄ /rGO/PDIP Z-scheme heterojunction, *Adv. Mater.* 33 (2021), e2007479.

[40] Z. Zhong, J. Liu, X. Xu, A. Cao, Z. Tao, W. You, L. Kang, Synthesis of Z-scheme cobalt porphyrin/nitrogen-doped graphene quantum dot heterojunctions for efficient molecule-based photocatalytic oxygen evolution, *J. Mater. Chem. A* 9 (2021) 2404–2413.

[41] F. Zhang, Y. Ma, Y. Chi, H. Yu, Y. Li, T. Jiang, X. Wei, J. Shi, Self-assembly, optical and electrical properties of perylene diimide dyes bearing unsymmetrical substituents at bay position, *Sci. Rep.* 8 (2018) 1–11.

[42] Y. Li, X. Zhang, D. Liu, Recent developments of perylene diimide (PDI) supramolecular photocatalysts: a review, *J. Photochem. Photobiol. C* 48 (2021).

[43] B.D. Viezbicke, S. Patel, B.E. Davis, D.P. Birnie, Evaluation of the Tauc method for optical absorption edge determination: ZnO thin films as a model system, *Phys. Status Solidi* 252 (2015) 1700–1710.

[44] Y. Liu, J. Li, B. Zhou, S. Lv, X. Li, H. Chen, Q. Chen, W. Cai, Photoelectrocatalytic degradation of refractory organic compounds enhanced by a photocatalytic fuel cell, *Appl. Catal. B: Environ.* 111 (2012) 485–491.

[45] C. Xing, G. Yu, T. Chen, S. Liu, Q. Sun, Q. Liu, Y. Hu, H. Liu, X. Li, Perylenetetracarboxylic diimide covalently bonded with mesoporous g-C₃N₄ to construct direct Z-scheme heterojunctions for efficient photocatalytic oxidative coupling of amines, *Appl. Catal. B: Environ.* 298 (2021), 120534.

[46] G. Zhu, H. Wen, M. Ma, W. Wang, L. Yang, L. Wang, X. Shi, X. Cheng, X. Sun, Y. Yao, A self-supported hierarchical Co-MOF as a supercapacitor electrode with ultrahigh areal capacitance and excellent rate performance, *Chem. Commun.* 54 (2018) 10499–10502.

[47] Z. Xiao, D. Kong, J. Liang, B. Wang, R. Iqbal, Q.-H. Yang, L. Zhi, Structure controllable carbon matrix derived from benzene-constructed porous organic polymers for high-performance Li-S batteries, *Carbon* 116 (2017) 633–639.

[48] M. Mahalakshmi, S. Selvanayagam, S. Selvasekaranapandian, M.V.L. Chandra, P. Sangeetha, R. Manjuladevi, Magnesium ion-conducting solid polymer electrolyte based on cellulose acetate with magnesium nitrate (Mg(NO₃)₂·6H₂O) for electrochemical studies, *Ionics* 26 (2020) 4553–4565.